

The Heavy Photon Search Test Detector

M. Battaglieri^a, S. Boyarinov^b, S. Bueltmann^c, V. Burkert^b, A. Celentano^a, G. Charles^f, W. Cooper^d, C. Cuevas^b, N. Dashyan^e, R. DeVita^a, C. Desnault^f, A. Deur^b, H. Egriyan^b, L. Elouadrhiri^b, R. Essig^g, V. Fadeyev^h, C. Fieldⁱ, A. Freyberger^b, Y. Gershtein^j, N. Gevorgyan^e, F.-X. Girod^b, N. Grafⁱ, M. Grahamⁱ, K. Griffioen^k, A. Grillo^h, M. Guidal^f, G. Hallerⁱ, P. Hansson Adrian^{i,*}, R. Herbstⁱ, M. Holtrop^l, J. Jarosⁱ, S. Kaneta^b, M. Khandaker^m, A. Kubarovskyⁿ, V. Kubarovsky^b, T. Maruyamaⁱ, J. McCormickⁱ, K. Moffeitⁱ, O. Moreno^h, H. Nealⁱ, T. Nelsonⁱ, S. Niccolai^f, A. Odianⁱ, M. Oriunnoⁱ, R. Paremuzyan^e, R. Partridgeⁱ, S. K. Phillips^l, E. Rauly^f, B. Raydo^b, J. Reichert^j, E. Rindel^f, P. Rosier^f, C. Salgado^m, P. Schuster^o, Y. Sharabian^b, D. Sokhan^p, S. Stepanyan^b, N. Toro^o, S. Uemuraⁱ, M. Ungaro^b, H. Voskanyan^e, D. Walzⁱ, L. B. Weinstein^c, B. Wojtsekhowski^b

^aIstituto Nazionale di Fisica Nucleare, Sezione di Genova e Dipartimento di Fisica dell'Università, 16146 Genova, Italy

^bThomas Jefferson National Accelerator Facility, Newport News, Virginia 23606

^cOld Dominion University, Norfolk, Virginia 23529

^dFermi National Accelerator Laboratory, Batavia, IL 60510-5011

^eYerevan Physics Institute, 375036 Yerevan, Armenia

^fInstitut de Physique Nucléaire d'Orsay, IN2P3, BP 1, 91406 Orsay, France

^gStony Brook University, Stony Brook, NY 11794-3800

^hSanta Cruz Institute for Particle Physics, University of California, Santa Cruz, CA 95064

ⁱSLAC National Accelerator Laboratory, Menlo Park, CA 94025

^jRutgers University, Department of Physics and Astronomy, Piscataway, NJ 08854

^kThe College of William and Mary, Department of Physics, Williamsburg, VA 23185

^lUniversity of New Hampshire, Department of Physics, Durham, NH 03824

^mNorfolk State University, Norfolk, Virginia 23504

ⁿRensselaer Polytechnic Institute, Department of Physics, Troy, NY 12181

^oPerimeter Institute, Ontario, Canada N2L 2Y5

^pUniversity of Glasgow, Glasgow, G12 8QQ, Scotland, UK

Abstract

The Heavy Photon Search (HPS), an experiment to search for a hidden sector photon in fixed target electroproduction, is preparing for installation at the Thomas Jefferson National Accelerator Facility (JLab) in the Fall of 2014. As the first stage of this project, the HPS Test Run apparatus was constructed and operated in 2012 to demonstrate the experiment's technical feasibility and to confirm that the trigger rates and occupancies are as expected. This paper describes the HPS Test Run apparatus and readout electronics and its performance. In this setting, a heavy photon can be identified as a narrow peak in the e^+e^- invariant mass spectrum, above the trident background or as a narrow invariant mass peak with a decay vertex displaced from the production target, so charged particle tracking and vertexing are needed for its detection. In the HPS Test Run, charged particles are measured with a compact forward silicon microstrip tracker inside a dipole magnet. Electromagnetic showers are detected in a PbWO₄ crystal calorimeter situated behind the magnet, and are used to trigger the experiment and identify electrons and positrons. Both detectors are placed close to the beam line and split top-bottom. This arrangement provides sensitivity to low-mass heavy photons, allows clear passage of the unscattered beam, and avoids the spray of degraded electrons coming from the target. The discrimination between prompt and displaced e^+e^- pairs requires the first layer of silicon sensors be placed only 10 cm downstream of the target. The expected signal is small, and the trident background huge, so the experiment requires very large statistics. Accordingly, the HPS Test Run utilizes high-rate readout and data acquisition electronics and a fast trigger to exploit the essentially 100% duty cycle of the CEBAF accelerator at JLab.

Keywords: silicon, microstrip, tracking, vertexing, heavy photon, dark photon, electromagnetic calorimeter

1 **1. Introduction**

2 The heavy photon (A'), aka a “hidden sector” or
3 “dark” photon, is a massive particle which couples
4 weakly to electric charge by mixing with the Standard
5 Model photon [1, 2]. Consequently, it can be radiated
6 by electrons and subsequently decay into e^+e^- pairs, al-
7 beit at rates far below those of QED trident processes.
8 Heavy photons have been suggested by numerous be-
9 yond Standard Model theories [3], to explain the dis-
10 crepancy between theory and experiment of the muon’s
11 $g - 2$ [4], and as a possible explanation of recent as-
12 trophysical anomalies, e.g. [5, 6, 7]. Heavy photons
13 couple directly to hidden sector particles with “dark”
14 or “hidden sector” charge; these particles could consti-
15 tute all or some of the dark matter, e.g. [8, 9]. Current
16 phenomenology highlights the $20 - 1000 \text{ MeV}/c^2$ mass
17 range, and suggests that the coupling to electric charge,
18 ee , has ϵ in the range of $10^{-3} - 10^{-5}$. This range of pa-
19 rameters makes A' searches viable in medium energy
20 fixed target electroproduction [10], but requires large
21 data sets and good mass resolution to identify a small
22 mass peak above the copious QED background. At
23 small couplings, the A' become long-lived, so detection
24 of a displaced decay vertex can reject the prompt QED
25 background and boost experimental sensitivity.

26 The HPS experiment [11] is preparing for installa-
27 tion in Hall-B at JLab in the Fall of 2014. It searches
28 for electro-produced A' in interactions between elec-
29 trons and nuclei in a thin (0.25% R.L.) Tungsten target
30 foil. The electrons are supplied by the nearly contin-
31 uous JLab CEBAF beam with energy between 2.2 and
32 6.6 GeV. The HPS experiment uses both invariant mass
33 and secondary vertex signatures to search for A' decaying
34 into e^+e^- pairs. In the interesting mass and coupling
35 range, the decay products are boosted along the beam
36 axis with small opening angles and decay lengths rang-
37 ing from mm’s to tens of cm’s requiring HPS to operate
38 tracking detectors down to 15 mrad opening angle only
39 10 cm behind the target. It employs a $\approx 1 \text{ m}$ long silicon
40 tracking and vertexing detector inside a dipole magnet
41 to measure and vertex charged particle trajectories and
42 a fast electromagnetic calorimeter just downstream of
43 the magnet to provide a trigger and identify electrons.
44 To overcome the background occupancy from multiple
45 scattered beam electrons both detectors have excellent
46 timing resolution and the experiment utilizes very high-
47 rate front-end electronics and runs at high trigger rates,

48 exploiting the 499 MHz bunch structure, 100% duty cy-
49 cle, of the JLab CEBAF accelerator to accumulate the
50 needed statistics.

51 The HPS Test Run, using a simplified version of the
52 HPS apparatus, was proposed and approved at JLab as
53 the first stage of HPS. Its purposes included demonstra-
54 ting that the apparatus and data acquisition systems are
55 technically feasible and the trigger rates and occupan-
56 cies to be encountered in electron-beam running are as
57 simulated. Given dedicated running time with electron
58 beams, the HPS Test Run apparatus is capable of search-
59 ing for heavy photons in unexplored regions of param-
60 eter space. Therefore, key design criteria and require-
61 ments for HPS and the HPS Test Run apparatus are the
62 same:

- 63 • uniform acceptance between 15 and ≈ 70 mrad in
64 the forward region to catch boosted decay products
65 close to the beam,
- 66 • beam passage through the apparatus in vacuum, to
67 eliminate direct interactions with the detector and
68 minimize beam gas interactions,
- 69 • detector components that can survive and effi-
70 ciently operate in a high radiation environment
71 with local doses exceeding 100 Mrad,
- 72 • high-rate electronics with trigger rates up to
73 50 kHz and data handling rates of 100 MB/s to per-
74 manent storage,
- 75 • a flexible, redundant and efficient trigger selecting
76 electron and positron pairs at rates up to 50 kHz,
- 77 • hit reconstruction efficiency higher than 99% and
78 average track reconstruction efficiency higher than
79 98% for electrons and positrons,
- 80 • excellent hit time resolution to reject out-of-time
81 background hits in the nearly continuous CEBAF
82 beam; 2 ns for hits on tracks in a 8 ns trigger win-
83 dow,
- 84 • momentum and angular resolution better than
85 4.5% and 1 to 4 mrad (across the track momen-
86 tum range in non-bend direction), respectively, to
87 reach A' mass resolution of 2.5% or less across the
88 interesting mass range,
- 89 • resolution of distance of closest approach to the
90 beam axis less than 250 (100) μm for tracks with
91 0.5 (1.7) GeV/c momentum to achieve a Gaussian
92 vertex resolution down to 1 mm at high masses
93 to discriminate displaced A' decays from prompt
94 QED backgrounds,

*Corresponding author.

Email address: phansson@slac.stanford.edu (P. Hansson
Adrian)

95 The HPS Test Run apparatus was installed on April 144
96 19, 2012, and ran parasitically in the photon beam of 145
97 the HDice experiment [12] until May 18. The JLab run 146
98 schedule precluded any dedicated electron beam run- 147
99 ning, but the HPS Test Run was allowed a short (\approx 6h) 148
100 and valuable dedicated photon beam run at the end of 149
101 scheduled CEBAF running. During this dedicated pe- 150
102 riod, e^+e^- pairs, produced in a gold foil upstream of the 151
103 experiment, where studied. With no dedicated electron 152
104 beam running no search for A' signal was possible but 153
105 this final running provided enough data to demonstrate 154
106 the functionality of the apparatus, document its perfor- 155
107 mance, and explore trigger rates, as shown below. 156

108 This paper reviews the HPS Test Run apparatus, doc- 157
109 umenting the performance of the trigger, data acquisi- 158
110 tion, silicon tracking and vertex detector, and the elec- 159
111 tromagnetic calorimeter at, or close to, the level re- 160
112 quired for calculating the physics reach of the HPS ex- 161
113 periment.

114 2. Detector Overview

115 The HPS Test Run apparatus was designed to run 162
116 in Hall B at JLab using the CEBAF 499MHz electron 163
117 beam at energies between 2.2 and 6.6 GeV and cur- 164
118 rents between 200 and 600 nA. The overall design of 165
119 the experiment follows from the kinematics of A' pro- 166
120 duction which typically results in a final state particle 167
121 within a few degrees of the incoming beam, especially 168
122 at low $m_{A'}$. Detectors must therefore be placed close 169
123 to the beam. The intense electron beam enlarges down- 170
124 stream after multiple scattering in the target and elec- 171
125 trons which have radiated in the target disperse horizon- 172
126 tally in the field of the analyzing magnet. Together they 173
127 constitute a “wall of flame” which must be completely 174
128 avoided. Accordingly, the apparatus is split vertically 175
129 to avoid a “dead zone”, the region within ± 15 mrad of 176
130 the beam plane. In addition, the beam is transported in 177
131 vacuum through the tracker to minimize beam-gas inter- 178
132 action backgrounds. Even with these precautions, the 179
133 occupancies of sensors near the beam plane are high, 180
134 dominated by the multiple Coulomb scattering of the 181
135 primary beam, so high-rate detectors, a fast trigger, and 182
136 excellent time tagging are required to minimize their 183
137 impact. The trigger comes from a highly-segmented 184
138 lead-tungstate ($PbWO_4$) crystal calorimeter located just 185
139 downstream of the dipole magnet. 186

140
141 A rendering of the apparatus installed on the beam line 190
142 is shown in Figure 1 and an overview of the coverage, 191
143 segmentation and performance is given in Table 1. 192

144 The silicon tracking and vertexing detector for the 145
145 HPS Test Run, or SVT, resides in a vacuum cham- 146
146 ber inside the Pair Spectrometer (PS) dipole magnet in 147
147 Hall B at JLab. The magnetic field strength was 0.5 T 148
148 oriented vertically throughout the run. The SVT has 149
149 five measurement stations, or “layers,” beginning 10 cm 150
150 downstream of the target. Each layer comprises a pair 151
151 of closely-spaced silicon microstrip sensors responsi- 152
152 ble for measuring a single coordinate, or “view”. In- 153
153 troduction of a small (50 or 100 mrad) stereo angle 154
154 between the two sensors of each layer provides three- 155
155 dimensional tracking and vertexing throughout the ac- 156
156 ceptance of the detector. In order to accommodate the 157
157 dead zone, the SVT is built in two halves that are ap- 158
158 proximately mirror reflections of one another about the 159
159 plane of the nominal electron beam. Each layer in one 160
160 half is supported on a common support plate with inde- 161
161 pendent cooling and readout.

162 The electromagnetic calorimeter (ECal) is also split 163
163 into two halves. Each half of the ECal consists of 221 164
164 $PbWO_4$ crystals arranged in rectangular formation. 165
165 There are five rows with 46 modules in each row except 166
166 the row closest to the beam plane which has 37. The 167
167 light from each crystal is read out by an Avalanche Photo- 168
168 diode (APD) glued on the back surface of the crys- 169
169 tal. Signals from the APDs are amplified using custom- 170
170 made amplifier boards before being sent to the data ac- 171
171 quisition electronics.

172 The Data Acquisition system combines two architec- 173
173 tures, the Advanced Telecom Communications Archi- 174
174 tecture (ATCA) based SVT readout system and VME- 175
175 bus Switched Serial (VXS) based digitization and trig- 176
176 gering system for the ECal.

177 3. The HPS Test Run Beamline

178 Since an electron beam was unavailable, the HPS Test 179
179 Run detected the electrons and positrons produced by 180
180 interactions of the secondary photon beam with a thin 181
181 foil just upstream of the detectors. The HPS Test Run 182
182 studied the performance of the detectors and the mul- 183
183 tiple coulomb scattering of the electrons and positrons. 184
184 Figure 2 shows the layout of the setup on the beam line. 185
185 The SVT was installed inside the Hall B pair spectrom- 186
186 eter magnet vacuum chamber with the ECal mounted 187
187 downstream of it. Both the SVT and the ECal were 188
188 retracted off the beam plane compared to nominal elec- 189
189 tron beam running to allow clean passage of the photon beam 190
190 through the system.

191 The photon beam was generated in the interaction of 192
192 5.5 GeV electrons with a $10^{-4} X_0$ gold radiator located

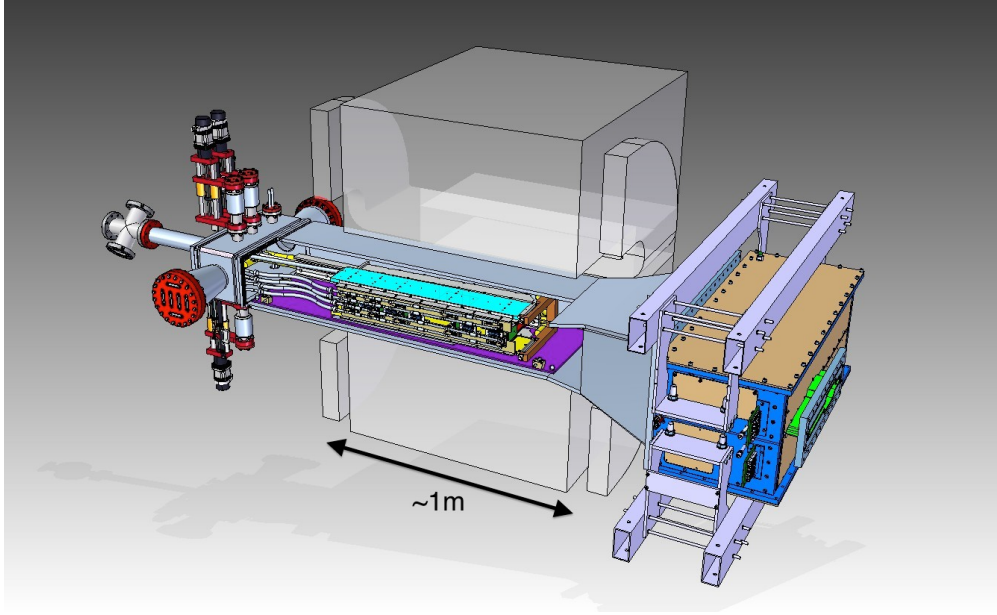


Figure 1: Rendering of the HPS Test Run apparatus installed on the beam line.

Table 1: Overview of the coverage, segmentation and performance of the HPS Test Run detector. The σ_{d_0} is the track impact parameter resolution of the SVT at the nominal electron target position. σ_{pos} is the estimated position resolution perpendicular to the strip direction on the silicon sensors of the SVT.

System	Coverage (mrad)	# channels	ADC (bit)	# layers	Segmentation	Time resolution (ns)	Performance
SVT	$15 < \theta_y < 70$ (5 hits)	12780	14	5 (stereo layers)	$30 \mu\text{m}$ (sense) $60 \mu\text{m}$ (readout) ($\sigma_{pos} \approx 6 \mu\text{m}$)	2.5	$\sigma_{d0,y} \approx 100 \mu\text{m}$ $\sigma_{d0,x} \approx 300 \mu\text{m}$ $\sigma_{d0,z} \approx 1 \text{ mm}$
ECal	$15 < \theta_y < 60$	442	12	1	$1.33 \times 1.33 \text{ cm}^2$ $1.6 \times 1.6 \text{ cm}^2$	4 (trigger)	$\sigma(E)/E \approx 4.5\%/\sqrt{E}$ Ref. [13, 14, 15]

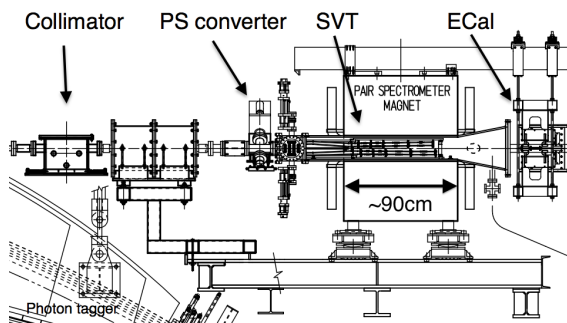


Figure 2: Layout of the HPS parasitic run.

193 $\approx 9 \text{ m}$ upstream of the PS. The primary beam and scattered electrons are deflected away from detectors by the
 194 dipole magnet of the photon tagging system. During the
 195 dedicated HPS Test Run period, the collimated (6.4 mm
 196 diameter) photon beam passes through the PS pair con-
 197 verter gold foil and later the HPS system. The PS pair
 198 converter was located $\approx 77 \text{ cm}$ upstream of the first layer
 199 of the SVT.
 200

201 Data was taken on three different converter thick-
 202 nesses with photon fluxes between 0.4 and $1.3 \times 10^8 \text{s}^{-1}$
 203 at photon energies between 0.55 and 5.5 GeV produced
 204 by a 30 to 90 nA electron beam. Data was measured
 205 for both polarities of the PS dipole magnet. The photon
 206 beam line during the HPS Test Run produced a rela-
 207 tively large number of e^+e^- pairs originating upstream
 208 of the converter position. This contribution was mea-
 209 sured during data taking with “empty” converter runs,

Converter thickn. (% X_0)	Duration (s)	e^- on radiator (μ C)
0	1279	88.1
0.18	2640	193.5
0.45	2149	140.7
1.6	911	24.4

Table 2: Measured integrated currents for the dedicated photon runs.

i.e. removing the converter but with all other conditions the same. The runs taken during the time dedicated to HPS Test Run are summarized in Table 2.

4. Silicon Vertex Tracker

The Silicon Vertex Tracker (SVT) enables efficient reconstruction of charged particles and precise determination of their trajectories. This allow A' decays to be distinguished from background via simultaneous measurements of the invariant mass of e^+e^- decay products and the position of decay vertices downstream of the target.

The design of the SVT is primarily driven by direct physics requirements and constraints from the environment at the interaction region. The A' decay products have momenta in the range of 0.4-2.0 GeV/c, so multiple scattering dominates mass and vertexing uncertainties for any possible material budget. The SVT must therefore minimize the amount of material in the tracking volume. The signal yield for long-lived A' is very small, so the rejection of prompt vertices must be exceedingly pure, on the order of 10^{-7} , in order to eliminate all prompt backgrounds. To achieve the required vertexing performance the first layer of the SVT must be placed no more than about 10 cm downstream of the target. At that distance, it is found that the active region of a sensor can be placed as close as 1.5 mm from the center of the beam, defining the 15 mrad “dead zone” mentioned previously, to maximize low-mass A' acceptance with decay products nearly collinear with the beam axis. At the edge of this “dead zone”, the radiation dose approaches 10^{15} electrons/cm²/month, or roughly 3×10^{14} 1 MeV neutron equivalent/cm²/month [16], requiring the sensors to be actively cooled. Meanwhile, very low-energy delta rays from beam-gas interactions would multiply the density of background hits, so the SVT must operate inside the beam vacuum. Finally, in order to protect the sensors, the detector must be movable so that it can be retracted during periods of uncertain beam conditions or beam tuning.

The mass resolution need to be around 2.5% across the interesting mass range to discover the A' signal on top of the copious QED background in the bump-hunt search. With A' decay opening angles between 15-70 mrad this translates into track momentum and angular resolution of 4-5% and 1-4 mrad (across the momentum range in the non-bend plane which dominates the measurement) [11]. With multiple scattering dominating both mass and vertexing uncertainties, spatial hit resolution less than 50 μ m are required in the non-bend plane in the first few layers which dominates the vertexing performance and about twice that in the non-bend plane.

High background occupancies, up to 4 MHz/mm² locally, in the region closest to the beam result from beam electrons undergoing multiple scattering in the target. These background hits are rejected by requiring the time reconstruction of each hit to be better than 2 ns.

4.1. Layout

The layout of the SVT is summarized in Table 3 and rendered in Figure 3. Each of the layers is comprised of a pair of closely-spaced silicon microstrip sensors mounted back- to-back to form a module. A 100 mrad stereo angle is used in the first three layers to provide higher- resolution 3D space points for vertexing. Using 50 mrad in the last two layers breaks the tracking degeneracy of having five identical layers and minimizes fakes from ghost hits to improve pattern recognition. Altogether, the SVT has 20 sensors for a total of 12780 readout channels.

Layer	1	2	3	4	5
z from target (cm)	10	20	30	50	70
Stereo angle (mrad)	100	100	100	50	50
Bend res. (μ m)	\approx 60	\approx 60	\approx 60	\approx 120	\approx 120
Non-bend res. (μ m)	\approx 6	\approx 6	\approx 6	\approx 6	\approx 6
# of sensors	4	4	4	4	4
Dead zone (mm)	\pm 1.5	\pm 3.0	\pm 4.5	\pm 7.5	\pm 10.5
Power cons. (W)	6.9	6.9	6.9	6.9	6.9

Table 3: Layout of the SVT.

The SVT is built in two separate halves that are mirror reflections of one another about the plane of the nominal electron beam. Each half consists of five modules mounted on a support plate that provides services to the modules and allows them to be moved as a group relative to the dead zone. The two halves of the tracker

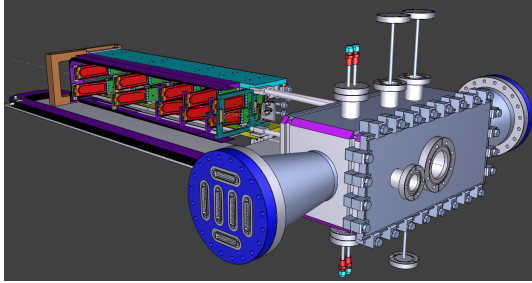


Figure 3: A rendering of the SVT showing the modules on their support plates held by the hinged C-support on the left and the motion levers on the right. The sensors are shown in red and the hybrid readout boards in green. The beam enters from the right through a vacuum box with flanges for services.

are connected to hinges mounted on a C-shaped support just beyond the last layer that defines the nominal spacing between the upper and lower halves of the tracker. A shaft attached to each support plate in front of layer one extends upstream and connects to a linear shift that transfers motion into the vacuum box through bellows to open and close the two halves around the dead zone. The C-support is mounted to an aluminum baseplate that defines the position of the SVT with respect to the vacuum chamber. Figure 4 shows a photograph of both completed detector halves prior to final assembly.



Figure 4: Both halves of the HPS Test Run SVT after final assembly at SLAC. The cooling manifolds and integrated cable runs are clearly seen.

297

298 4.2. Components

299 The sensors for the SVT are $p+$ -on- n , single-sided,
300 AC-coupled, polysilicon-biased microstrip sensors fab-
301 ricated on $<100>$ silicon and have 30 (60) μm sense
302 (readout) pitch over their $4 \times 10 \text{ cm}^2$ surface. This

303 sensor technology was selected to match the require-
304 ment of $< 1\% X_0$ per layer, single-hit resolution bet-
305 ter than 50 μm and tolerance of a radiation dose of ap-
306 proximately $1.5 \times 10^{14} 1 \text{ MeV}$ neutron equivalent/ cm^2
307 for a six month run. The sensors, produced by Ham-
308 matsu Photonics Corporation, were originally meant
309 for the cancelled Run 2b upgrade of the DØ exper-
310 iment [17] which satisfied the requirement that the
311 technology must be mature and available within the time and
312 budget constraints.

313 Despite having only small spots with very high occu-
314 pancy (up to 4 MHz/mm²) closest to the primary beam,
315 the rates are still high and lowering the peak occupancy
316 to approximately 1% for tracking requires a trigger win-
317 dows and hit time tagging of roughly 8 ns. The ECal
318 readout and trigger described in Sec. 5.3 can achieve
319 such resolution. To reach this performance the sen-
320 sors for the SVT are readout by the APV25 ASIC de-
321 veloped for the CMS experiment at CERN [18]. The
322 APV25 can capture successive samples of the shaper
323 output in groups of three at a sampling rate of approx-
324 imately 40 MHz. By fitting the known $CR-RC$ shaping
325 curve to these samples, the initial time of the hit can
326 be determined to a precision of 2 ns for S/N≈25 [19].
327 For electron beam running, six-sample readout and the
328 shortest possible shaping time (35 ns) is used to best
329 distinguish hits that overlap in time. The APV25 ASICS
330 are hosted on simple FR4 hybrid readout boards, out-
331 side the tracking volume, with a short twisted-pair pig-
332 tail cable to provide power and configuration and signal
333 readout. Along with a single sensor, these are glued
334 to a polyimide-laminated carbon fiber composite back-
335 ing making up a half-module. A window is machined
336 in the carbon fiber leaving only a frame around the pe-
337 riphery of the silicon to minimize material. A 50 μm
338 sheet of polyamide is laminated to the surface of the
339 carbon fiber with 1 mm overhang at all openings to en-
340 sure good isolation between the back side of the sensor,
341 carrying high-voltage bias, and the carbon fiber which
342 is held near ground.

343 The sensor modules for the SVT consist of a pair
344 of identical half-modules, sandwiched back-to-back
345 around an aluminum cooling block at one end and a sim-
346 ilar PEEK spacer block at the other. Figure 5 shows a
347 single module after assembly. The cooling block pro-
348 vides the primary mechanical support for the module as
349 well as cooling via copper tubes pressed into grooves
350 in the plates. The spacer block defines the spacing be-
351 tween the sensors at the far end of the module, stiffens
352 the module structure, and improves the stability of the
353 sensor alignment. The average support material in the
354 tracking volume is approximately 0.06% X_0 per double-

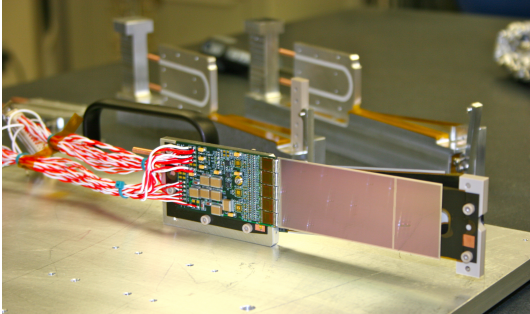


Figure 5: A prototype module assembly (foreground) with the 50 mrad (left) and 100 mrad (right) module assembly fixtures in the background. A pair of cooling blocks and a spacer block can be seen on the fixtures.

sided module for a total material budget of 0.7% per layer.

The total SVT power consumption budget of about 50 W is removed by a water/glycol mixture circulated through a flexible manifold attached to the copper tubes in the cooling blocks. During the HPS Test Run the sensors were operated at around 23° C. The power consumption is dominated by five APV25 ASICs on each hybrid board consuming approximately 2 W, radiant heat load is less than 0.5 W per sensor and leakage current is only significant in a small spot after irradiation.

4.3. Production, Assembly and Shipping

Hybrids with APV25 ASICs underwent quick qualification testing and each half-module was run at low temperature ($\approx 5^\circ \text{C}$) and fully characterized for pedestals, gains, noise and time response after assembly. Of 29 half-modules built, 28 passed qualification testing, leaving eight spare modules after completion of the SVT. Only sensors capable of 1000 V bias voltage without breakdown were used. Full-module assembly and mechanical surveys were performed at SLAC before final assembly, testing and shipping of the SVT to JLab. A custom shipping container with nested crates and redundant isolation for shock and vibration was built in order to safely send the partly assembled SVT to JLab. At JLab, the entire SVT was integrated with the full DAQ and the power supplies before moving the module-loaded support plates to Hall B for final mechanical assembly and installation inside of the vacuum chamber.

4.4. Alignment

The SVT was aligned using a combination of optical, laser and touch probe surveys at SLAC and JLab. The

optical survey of individual modules with a precision of a few μm was combined with a touch-probe survey of the overall SVT support structure, with 25-100 μm precision, to locate the silicon sensor layers with respect to the support plates and the mechanical survey balls on the base plate. After full assembly and installation of the SVT at JLab, a mechanical survey of the SVT base plate position inside the pair spectrometer vacuum chamber is used to determine the global position of the SVT with respect to the CEBAF beam line. The resulting survey-based alignment has the position of the silicon sensors correct to within a few hundred microns measured from tracks in the HPS Test Run data. A more sophisticated global track-based alignment technique to reach final alignment precision well below 50 μm is being developed.

5. Electromagnetic Calorimeter

The electromagnetic calorimeter (ECal), installed downstream of the PS dipole magnet, performs two essential functions for the experiment: it provides a trigger signal to select what events to read out from the detector sub-systems and is used in the analysis to identify electrons and positrons. The technology and design choices are largely driven by the need for a compact forward design covering the SVT A' acceptance and able to fully absorb electrons and positrons with energy between 0.5-6.5 GeV. It needs granularity and signal readout speed to handle 1 MHz/cm² of electromagnetic background and to be radiation hard. While the signal A' trigger is largely insensitive to the energy resolution, in order to have the possibility to improve the energy resolution from the SVT measurement $\sigma(E)/E < 4.5\%/\sqrt{E}$ is needed.

The PbWO₄ crystal inner calorimeter of the CLAS detector [13, 14, 15], in operation since 2005 in Hall B, meets all the requirements set by HPS. The modules from this calorimeter have been subsequently repurposed for HPS.

5.1. Components

The ECal module shown in Figure 6 is based on a tapered 160 mm long PbWO₄ crystal with a 13.3 × 13.3 mm² (16 × 16 mm²) front (rear) face wrapped in VM2000 multilayer polymer mirror film. The scintillation light yield, approximately 120 photons/MeV, is read out by a 5×5 mm² Hamamatsu S8664-55 Avalanche Photodiode (APD) with 75% quantum efficiency glued to the rear face surface using MeltMount 1.7 thermal plastic adhesive. This results in about 8

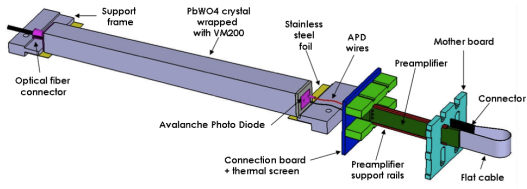


Figure 6: A schematic view of an ECal module.

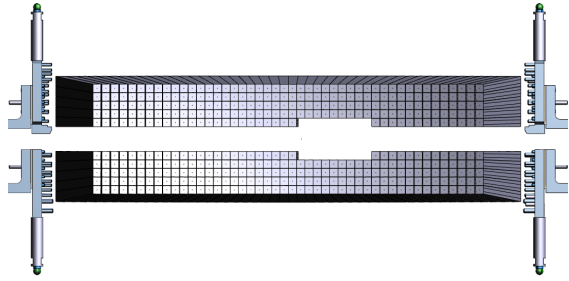


Figure 7: Rendered layout view of the ECal looking downstream.

435 photoelectrons/MeV which needs to be amplified before
 436 fed into the FADC for digitization and processing. The
 437 maximum energy deposited in a crystal is expected to
 438 be 4.2 GeV which needs to match the input range of the
 439 FADC. The relatively low gain of the APD (~ 200) was
 440 compensated with custom-made preamplifier boards,
 441 that provide further amplification to match the 2 V dy-
 442 namic range of the FADC. With a total noise level of
 443 about 10 MeV and a resolution of about 1 ADC/MeV
 444 the ADC resolution fulfills the requirements from HPS.

445 5.2. Layout

446 Similar to the SVT, the ECal is built in two separate
 447 halves that are mirror reflections of one another about
 448 the plane of the nominal electron beam to avoid inter-
 449 ferring with the 15 mrad “dead zone”. As shown in Fig-
 450 ure 7, the 221 modules in each half, supported by alu-
 451 minum support frames, are arranged in rectangular for-
 452 mation with five layers and 46 crystals/layer except for
 453 the layer closest to the beam where nine modules were
 454 removed to allow a larger opening for the outgoing elec-
 455 tron and photon beams. Each half was enclosed in a
 456 temperature controlled box ($< 1^\circ \text{F}$ stability and $< 4^\circ \text{F}$
 457 uniformity) to stabilize the crystal light yield and the op-
 458 eration of the APDs and its preamplifiers. Four printed
 459 circuit boards mounted on the backplane penetrated the
 460 enclosure and were used to supply the ± 5 V operating
 461 voltage for the preamplifiers, 400 V bias voltage to the
 462 APDs, and to read out signals from the APDs. Each half
 463 of the ECal was divided into 12 bias voltage groups with
 464 a gain uniformity of about 20%.

465 During the HPS Test Run, both halves were held in
 466 place by four vertical bars attached to a rail above, plac-
 467 ing the front face of the crystals 147 cm from the up-
 468 stream edge of the magnet, with a 8.7 cm gap between
 469 the innermost edge of the crystals in the two halves.

470 5.3. Signal readout

471 After a 2:1 signal splitter, 1/3 of an amplified APD
 472 signal was fed to a single channel of a JLab flash ADC
 473 (FADC) board [20]. 2/3 of the signal was sent to a

474 discriminator module and then to a TDC for a timing
 475 measurement. The FADC boards are high speed VXS
 476 modules digitizing up to 16 APD signals at 250 MHz
 477 and storing samples in $8 \mu\text{s}$ deep pipelines with 12-bit
 478 resolution. When a trigger is received, the part of the
 479 pipeline from 5 samples before and 30 after the signal
 480 which crossed a programmable threshold (for the HPS
 481 Test Run this was set to ≈ 70 MeV) are summed and
 482 stored in a 17-bit register for readout. In addition a
 483 4 ns resolution timestamp of the threshold crossing is
 484 reported in the readout for each pulse. This scheme
 485 significantly compresses the data output of the FADC.
 486 During offline data analysis, a calibrated pedestal value
 487 is subtracted to obtain the actual summed energy. Two
 488 20-slot VXS crates with 14 (13) FADC boards were em-
 489 ployed in the HPS Test Run to read out the top (bottom)
 490 half of the ECal.

491 6. Trigger and Data Acquisition

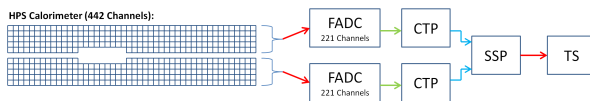
492 The DAQ system handles acquisition of data from the
 493 ECal and SVT sub-detectors with two DAQ architec-
 494 tures. The SVT DAQ is based on Advanced Telecom
 495 Communications Architecture (ATCA) hardware while
 496 the ECal uses VMEbus Switched Serial (VXS) based
 497 hardware. Data from the sub-detectors are only read
 498 out when a trigger signal from the trigger system is re-
 499 ceived.

500 6.1. Trigger system

501 The trigger system is designed to select time coinci-
 502 dences of electromagnetic clusters in the top and bot-
 503 tom halves of the ECal satisfying loose kinematic selec-
 504 tions optimized on A' events to further reduce the rate.
 505 The trigger system need to be essentially dead time free,
 506 handle rates up to 50 kHz and importantly supply a trig-
 507 ger time relative to the beam bunches with 8 ns to reduce

508 the background from out-of-time hits in the high occu-
 509 pancy regions of the SVT. Figure 8 shows a schematic
 510 overview of each stage of the system. Each channel on
 511 the FADC board has an independent data path to send 5-
 512 bit pulse energy and 3-bit pulse arrival time information
 513 every 32 ns to a trigger processing board (CTP), which
 514 is in the same crate. The 3-bit pulse arrival time allows
 515 the trigger to know the pulse timing at 4 ns resolution.
 516 Contrary to the readout path described in Sec. 5.3, this
 517 energy is a pedestal-subtracted time-over-threshold sum
 518 with programmable offsets and minimum threshold dis-
 519 criminator for each channel. With input from all FADC
 520 channels, i.e. one half of the ECal, the CTP performs
 521 cluster finding and calculates cluster energy and tim-
 522 ing information. The 3x3 fixed-window, highly parallel,
 523 FPGA-based cluster algorithm simultaneously searches
 524 for up to 125 clusters with energy sum larger than the
 525 programmable energy threshold (\approx 270 MeV). Crystals
 526 in the fixed-window are included in the sum if the lead-
 527 ing edge of the pulse occurred within a 32 ns time win-
 528 dow to take into account clock skew and jitter through-
 529 out the system. The CTP only accepts clusters with the
 530 locally highest energy 3x3 window to deal with over-
 531 lapping and very large clusters. The sub-system board
 532 (SSP) receives the clusters from the top and bottom half
 533 CTP at a maximum of 250MHz and searches for pairs
 534 of clusters in an 8 ns wide coincidence window. The
 535 SSP sends triggers to the trigger supervisor (TS), which
 536 generates all the necessary signals and controls the en-
 537 tire DAQ system readout through the trigger interface
 538 units installed in every crate that participate in the read-
 539 out process.

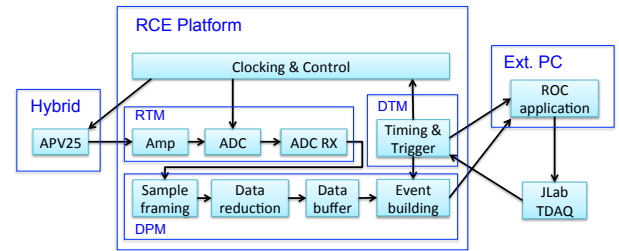
540 The trigger system is free-running and driven by the
 541 250 MHz global clock and has essentially zero dead
 542 time at the occupancies expected for HPS. The trigger
 543 supervisor can apply dead time if necessary, for example
 544 on a ‘busy’ or ‘full’ condition from the front-end elec-
 545 tronics. The system is designed to handle trigger rates



546 Figure 8: Block diagram of the ECAL trigger system consisting
 547 of the FADC that samples and digitizes signals for each detec-
 548 tor channel and sends them for cluster finding in the CTP. The
 549 CTP clusters are sent to the SSP where the final trigger deci-
 550 sion is taken based on pairs of clusters in both halves of the
 551 ECal. The decision is sent to the Trigger Supervisor (TS) that
 552 generates the necessary signals to read out the sub-detectors.



553 Figure 9: The SVT DAQ COB board with four data processing
 554 daughter cards (DPMs) visible on the left side.



555 Figure 10: Block diagram overview of the SVT DAQ.

556 above 50 kHz and has a latency set to $\approx 3 \mu\text{s}$ to match
 557 that required by the SVT APV25 ASIC.

558 During the HPS Test Run, for the most part the trigger
 559 system required only a single cluster in either the top or
 560 bottom ECal halves but was tested to trigger rates above
 561 100 kHz by lowering thresholds.

562 6.2. SVT Data Acquisition

563 The purpose of the SVT DAQ is to support the con-
 564 tinuous 40 MHz readout and processing of signals from
 565 each of the 20 silicon strip sensors of the SVT. The data
 566 for each strip channel, six analog samples of the sig-
 567 nal, needs to be transferred to the JLab DAQ for those
 568 events selected by the trigger at rates up to 50 kHz and
 569 with data transfer rates up to 100 MB/s.

570 The SVT DAQ is based on the Reconfigurable Clus-
 571 ter Element (RCE) and cluster interconnect concept de-
 572 veloped at SLAC as generic building blocks for DAQ
 573 systems. The RCE is a generic computational build-
 574 ing block, housed on a separate daughter card called
 575 Data Processing Module (DPM), that is realized on an
 576 ATCA front board called the Cluster On Board (COB),
 577 see Figure 9. The first generation RCE used in the HPS
 578 Test Run consisted of a Virtex 5 FPGA with 1 GB of
 579 DDR3 RAM. A schematic overview of the system is
 580 shown in Figure 10. The analog outputs of up to 12

571 SVT half-modules (60 APV25 ASICs) are digitized on 620
572 the Rear-Transition-Module (RTM), a custom board on 621
573 the back side of the ATCA crate, interfacing the HPS- 622
574 specific readout to the generic DAQ components on the 623
575 COB. A pre-amplifier converts the APV25 differential 624
576 current output to a different voltage output scaled to the 625
577 sensitive range of a 14-bit ADC operating at the system 626
578 clock of 41.667 MHz. The RTM is organized into four 627
579 sections with each section supporting three SVT half- 628
580 module hybrids (15 APV25 ASICs). The RTM also 629
581 includes a 4-channel fiber-optic module and supporting 630
582 logic which is used to interface to the JLab trigger 631
583 system supervisor. Each section of the RTM is input to a 632
584 DPM which apply thresholds for data reduction and 633
585 organizes the sample data into UDP datagrams. The DPM 634
586 also hosts an I²C controller used to configure and mon- 635
587 itor the APV25 ASICs. A single ATCA crate with two 636
588 COB cards was used, one supporting four DPMs and 637
589 one supporting three DPMs and one DPM that is con-
590 figured as the trigger and data transmission module. The
591 two COB cards and their DPMs are interconnected with
592 a 10 Gb/s switch card [21] which also hosts two 1Gb/s
593 Ethernet interfaces to the external SVT DAQ PC.

594 The external PC supports three network interfaces: 638
595 two standard 1 Gb/s Ethernet and one custom low- 639
596 latency data reception card. The first is used for slow 640
597 control and monitoring of the 8 DPM modules and the 641
598 second serves as the interface to the JLAB data acquisi- 642
599 tion system. The third custom low-latency network in- 643
600 terface is used to receive data from the ATCA crate and 644
601 supports a low latency, reliable TTL trigger acknowl- 645
602 edge interface to the trigger DPM. This PC hosts the 646
603 SVT control and monitoring software as well as the 647
604 Read Out Controller application used to interface with 648
605 the JLab DAQ.

606 In order to minimize cable length for the analog 649
607 APV25 output signal the ATCA crate was located ap- 650
608 proximately 1 m from the beam line, next to our ca- 651
609 ble vacuum feed-throughs. Before shielding with lead- 652
610 blankets was arranged, we observed two failures of 653
611 normally reliable ATCA crate power supplies, time- 654
612 correlated to beam instabilities.

613 Although trigger rates during the HPS Test Run were 655
614 significantly lower, this system was tested at trigger 656
615 rates up to 20 kHz and 50 MB/s. With optimized event 657
616 blocking and improved ethernet bandwidth, together 658
617 with utilizing the overlapping readout and trigger func- 659
618 tionality of the APV25, the system is capable of being 660
619 read out at 50 kHz trigger rate.

6.3. General Data Acquisition and Online Computing

Every crate participating in the readout process contains a Readout Controller (ROC) that collects digitized information, processes it, and sends it on to the event builder. For the ECal, both VXS crates run ROC applications in a single blade Intel-based CPU module running CentOS Linux OS. For the SVT DAQ, the ROC application runs on the external PC under RHEL. The event builder assembles information from the ROCs into a single event which is passed to the event recorder that writes it to a RAID5-based data storage system capable of handling up to 100 MB/s. The event builder and other critical components run on multicore Intel-based multi-CPU servers. The DAQ network system is a network router providing 10 Gb/s high-speed connection to the JLab computing facility for long-term storage. For the HPS Test Run, both the SVT and ECal ROC had a 1 Gb/s link to the network router.

7. Reconstruction and Performance

While dedicated electron beam was precluded for the HPS Test Run the short dedicated photon beam run allowed the study of some of the key performance parameters for HPS and also explore the expected trigger rates during electron beam running. This section documents the performance and discusses the results implication for HPS.

7.1. SVT Performance

For the duration of the HPS Test Run all SVT modules and APV25 chips were configured to their nominal operating points [22] with all sensors reverse-biased at 180 V. The sensors were operated within a temperature range of 20 – 24°C. Approximately 97% of the 12,780 SVT channels were found to be operating normally; the fraction of dead or noisy channels varied from 2.4% to 4.7% throughout the HPS Test Run. Most of these losses were due to 2-4 misconfigured APV25 ASICs, a known noisy half-module and problems in two particular APV25 ASICs.

7.1.1. Cluster and Hit Reconstruction

Track reconstruction in the SVT puts stringent requirement on the clustering and hit reconstruction. The multiple scattering in the tracking material dominates the uncertainty in the track parameter estimation and effectively determines the roughly 50 μm (200 μm) requirement on the spatial hit resolution in the non-bend (bend) plane. The high occupancy due to multiple scattered beam electrons in the target close to the beam requires a hit time resolution of 2 ns to efficiently reject

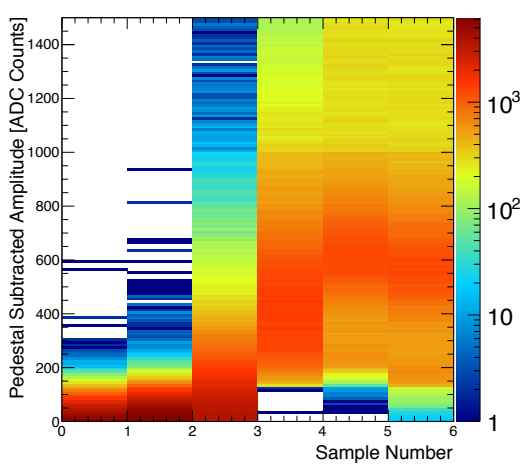


Figure 11: Accumulation of six pedestal-subtracted samples from individual SVT channels associated with hits on tracks.

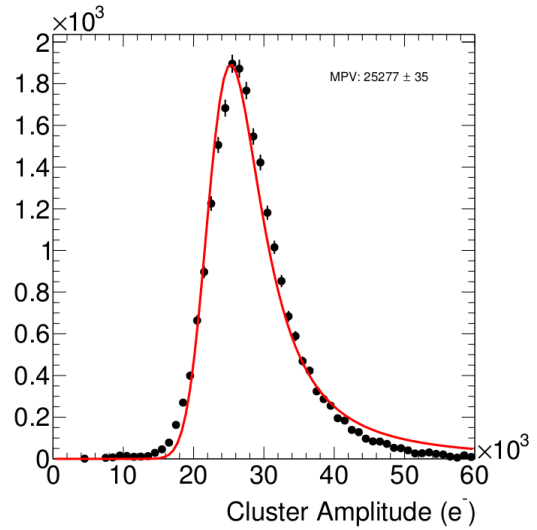


Figure 12: The cluster charge distribution for hits associated with a track follow the characteristic Landau shape.

668 out-of-time hits in HPS. Both the hit time, based on a
 669 fit to the APV25 ASIC pulse shape, and the spatial po-
 670 sition reconstruction rely on having S/N around 25 for
 671 the sensors used in HPS.

672 After a trigger is received, the amplitude of every
 673 APV25 analogue output is sampled and digitized in six
 674 consecutive time bins, separated by roughly 25 ns. A
 675 data reduction algorithm is applied requiring three out
 676 of six samples to be above two times the noise level and
 677 that the third sample is larger than the second or that
 678 the fourth sample is larger than the third. The typical,
 679 pedestal subtracted, pulse shape obtained is shown in
 680 Figure 11. As the figure demonstrates, the SVT was
 681 well timed-in to the trigger with the rise of the pulse at
 682 the 3rd sampling point. In order to find the time, t_0 , and
 683 amplitude of each hit, the six samples from each chan-
 684 nel are fitted to an ideal $CR - RC$ function. Note that
 685 in the HPS Test Run the APV25 ASICs were operating
 686 with a 50 ns shaping time. These hits are passed through
 687 a simple clustering algorithm which forms clusters by
 688 grouping adjacent strips with the position of a cluster on
 689 the sensor determined by the amplitude-weighted mean.
 690 With a linear gain up to ≈ 3 MIPs, the cluster charge
 691 for hits associated with a track follow the characteris-
 692 tic Landau shape, see Figure 12. A noise level between
 693 $1.1 - 1.5 \times 10^3$ electrons was established through mu-
 694 tiple calibration runs giving a signal to noise ratio of
 695 21 – 25, in line with the requirement for HPS. Lab-
 696 based radioactive source tests were used to provide the
 697 absolute charge normalization. After clustering hits on

698 a sensor, the hit time for each cluster is computed as the
 699 amplitude-weighted average of the individually fitted t_0
 700 on each channel. The t_0 resolution is studied by com-
 701 paring the cluster hit time with the average of all cluster
 702 hit times on the track shown in Figure 13. After cor-
 703 recting for offsets from each sensor (time-of-flight and
 704 clock phase) and accounting for the correlation between
 705 the t_0 and track time, the extracted t_0 resolution is 2.6 ns.
 706 This is somewhat worse than the approximately 2 ns res-
 707 olution expected for S/N=25 which we attribute to the
 708 true pulse shape differing from our idealized fit function
 709 which will be improved in the future [23]. Reducing the
 710 APV25 ASIC pulse shaping time to 35 ns will also im-
 711 prove time resolution. These results show that we can
 712 operate with the six sample readout mode of the APV25
 713 chip and achieve time resolution adequate for pileup re-
 714 jection during electron running in HPS.

715 Good agreement was obtained between observed and
 716 simulated occupancies after taking into account dead or
 717 noisy channels. The hit reconstruction efficiency was
 718 estimated by measuring the number of good tracks with
 719 a hit close to the extrapolated intersection of a given
 720 sensor that was excluded from the track fit itself. Tracks
 721 which intersect regions with known bad channels or
 722 pass very close to the edge region were excluded. The
 723 hit reconstruction efficiency, see Figure 14, was mea-
 724 sured to be above 98% and fairly uniform across the
 725 SVT.

726 The spatial resolution of similar microstrip sensors is

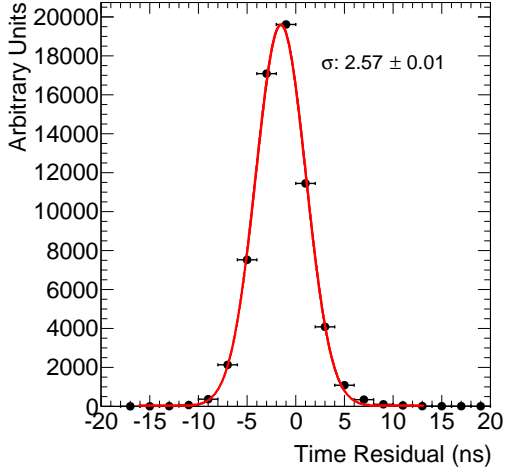


Figure 13: The residual of individual cluster times with the average of all clusters on the track.

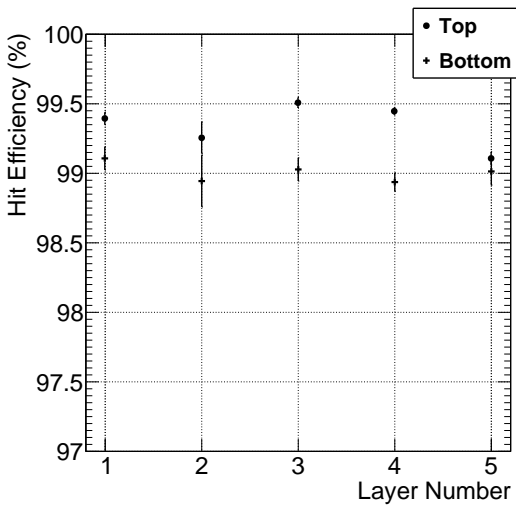


Figure 14: The hit reconstruction efficiency as a function of detector layer.

well established by test beam data, against which the charge deposition model in the simulation is validated. This resolution can be parameterized as a function of the total signal to single-strip noise and the crossing angle of tracks through the sensor. The single-hit resolution for charged particles with signal-to-noise ratio above 20, as demonstrated here, is relatively constant at approximately $6 \mu\text{m}$ for tracks that enter approximately normal to the sensors as in HPS. This resolution is significantly better than the requirement for reaching the mass and vertex resolutions required for HPS.

7.1.2. Momentum and Vertexing Resolution

Good track reconstruction performance is crucial to HPS. Simulations show that track momentum resolution of 4-5% is needed to reach the expected A' mass resolution. The precise reconstruction of the production vertex to reject prompt QED background requires impact parameter resolutions between $100\text{-}250 \mu\text{m}$ for tracks between $0.5\text{-}1.7 \text{ GeV}/c$. These key performance parameters were studied in the HPS Test Run by selecting e^+e^- pairs from photon conversions. Pairs of oppositely charged tracks, one in the top and one in the bottom half of the SVT, with momentum larger than $400 \text{ MeV}/c$ were selected and basic distributions of pair production kinematics were studied. The kinematics are relatively well reproduced as shown in Figure 15.

The expected momentum resolution from simulation is between 4-5% for tracks in the momentum range of the HPS Test Run. By comparing, between data and simulation, the shapes of the kinematic distributions for single- and two-track events, we estimate an agreement with the nominal scale and resolution to within 10%.

In the HPS Test Run, as well as in electron running with HPS, the dominant source of uncertainty in the tracking and vertexing is multiple Coulomb scattering. For the vertexing performance the foremost difference compared to electron beam running is that the target was located approximately 67 cm upstream from our nominal target position; giving almost collinear tracks in the detector. The increased lever arm over which tracks are extrapolated widens the resolution with up to a factor of eight (depending on momentum) compared to what is achieved at the nominal electron target position for HPS. Figure 16 shows the horizontal and vertical positions of the extrapolated track at the converter position. While residual alignments show small shifts, the good agreement between data and simulated events of the widths indicates a good understanding of the material budget and distribution in the SVT. Having the

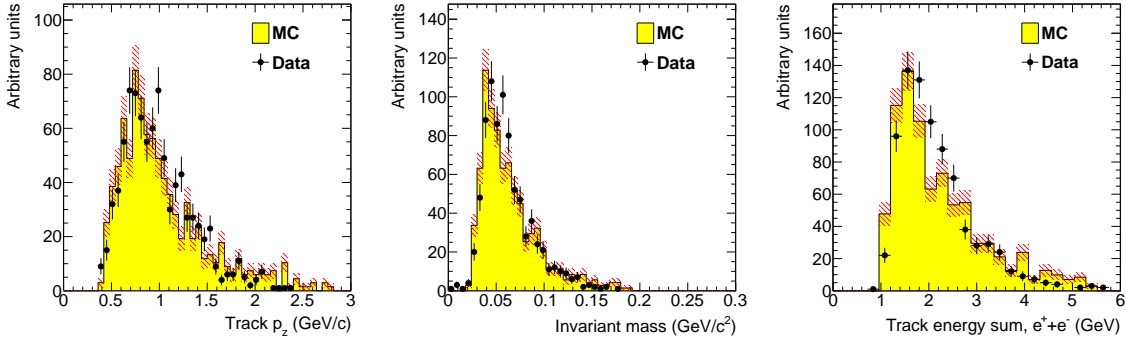


Figure 15: Kinematic distributions for e^+e^- pairs selected by opposite charged tracks in the top and bottom half of the tracker: track momentum in the top half of the SVT (left), invariant mass (middle) and the sum of the track energy for the pair (right).

777 dominant contribution to the vertex resolution approxi- 812
778 mately right demonstrates that the Gaussian part of the 813
779 vertex resolution in HPS, with a target at 10 cm, will be 814
780 as calculated.

781 7.2. ECal Performance

782 During the HPS Test Run 385 out of 442 modules 818
783 (87%) were used in offline reconstruction, 39 modules 819
784 were disabled or not read out (no FADC channel avail- 820
785 able, no APD bias voltage or masked out due to excess- 821
786 sive noise) and 18 were masked offline due to noise.

787 The integrated pulse of each FADC channel was con- 822
788 verted to energy by subtracting a pedestal and applying 824
789 a conversion factor to convert ADC counts to energy. 825
790 The pedestals are measured using special runs where 826
791 each trigger records 100 samples of signals from the 827
792 APDs with 4 ns between each sample. The pedestals 828
793 were extracted from the part of the window before the 829
794 actual hit in the calorimeter. Modules with signal above 830
795 the threshold are clustered using a simple algorithm
796 similar to the one deployed for the trigger (see Sec. 6.1).
797 Due to the high effective crystal readout threshold of
798 73 MeV the average number of crystals in a cluster was
799 ~ 3 and the simple clustering algorithm worked well for
800 reconstruction of the detected shower energy. An aver-
801 age noise level of approximately 15 MeV per crystal
802 was measured in special pedestal runs.

803 The ratio of the ECal cluster energy E to the momen- 837
804 tum p of a matched track in the SVT was used to de- 838
805 termine the conversion factors from ADC counts to en- 839
806 ergy. To compare data and simulation, all inoperable or 840
807 noisy channels in the SVT and ECal were disabled in 841
808 both data and simulation so that any efficiency or bias 842
809 that affect the data should be reflected in the simulation.
810 Iteratively, conversion coefficients for each crystal were 843
811 adjusted until the E/p ratio in data and simulation were 845

812 similar. The distribution of the E/p ratio in data and 813 simulation are compared in Figure 17. The peak position 814 of the distribution indicates the sampling fraction 815 of the ECal, the fraction of the incident particle energy 816 measured in the cluster. The width and tails of the distri- 817 bution in data indicates imperfect calibration and noise 818 of the ECal modules. This level of calibration and the 819 agreement with simulation was found to be sufficient to 820 study normalized event rates in the HPS Test Run.

821 Since the A' trigger in HPS is relatively insensitive 822 to the energy resolution this level of performance 823 would be adequate. However, improvements are needed 824 to achieve the expected energy resolution in HPS ($< 4.5\%/\sqrt{E}$). The noise and thresholds need to be 825 closer to 10 MeV the thresholds will be lowered and a 826 more elaborate calibration technique needs to be em- 827 ployed. In addition the number of working channels 828 needs to be improved by equipping the detector new and 829 complete electronics for each channel.

831 7.3. Trigger Performance

832 As described above in Sec. 6, the energy from each 833 crystal is measured differently in the trigger and what 834 is readout from the ECal. The trigger performance 835 was studied by simulating the trigger for each event 836 and comparing to how the events were actually trig- 837 gered. To eliminate trigger bias, we use a tag and probe 838 method: to study the trigger performance in one half 839 of the ECal, we select events which triggered the other 840 half and where there was exactly one probe cluster in 841 the ECal half under study. We then measure trigger ef- 842 ficiency as the fraction of tagged events that fired the 843 trigger in the probe half as a function of the probe clus- 844 ter energy, shown in Figure 18. The trigger turn-on is 845 slow and reaches an uneven plateau at about 700 MeV

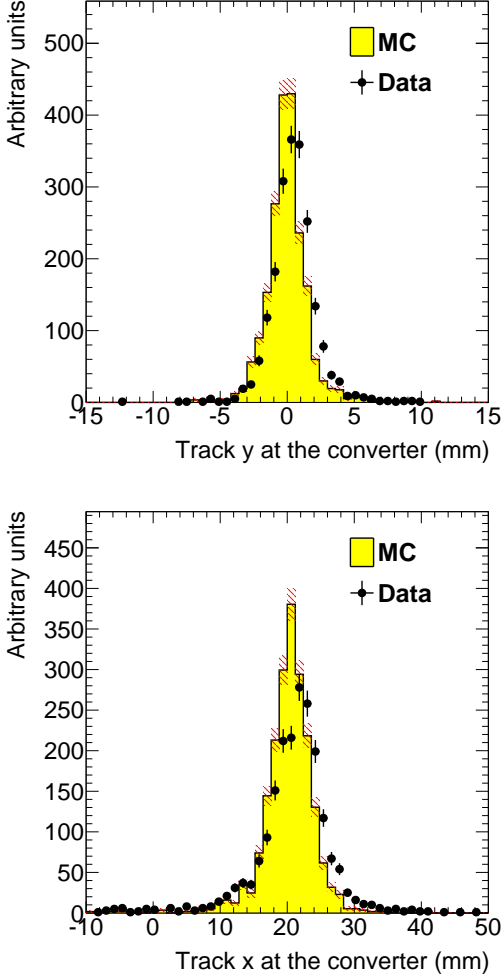


Figure 16: Vertical (top) and horizontal (bottom) extrapolated track position at the converter position taking into account the measured fringe field.

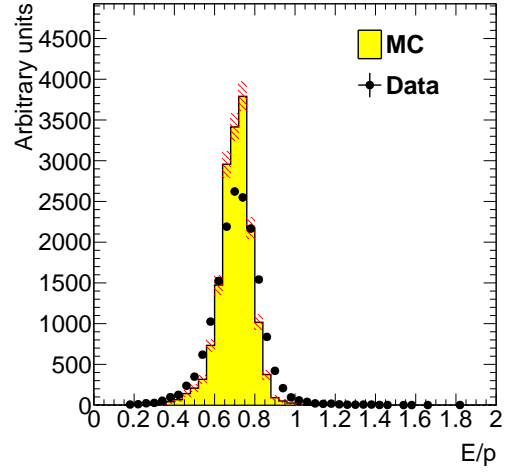


Figure 17: The ECal energy over track momentum ratio (E/p) comparing data and simulation for single cluster triggers in the top half of the ECal.

for two reasons; gain variations between different crystals lead to the threshold variations and the nonlinearity of the time-over-threshold integral means that the effective threshold is higher for clusters that span multiple crystals. The effective trigger threshold is therefore dependent on position and energy of the particle as well as cluster multiplicity.

As a cross-check we simulate the FADC trigger path by converting from readout hits (with fixed-size window integration) to trigger hits (time-over-threshold integration). The CTP clustering algorithm and the trigger decision from the SSP are simulated before we compare the trigger decision and trigger time to what was reported by the actual trigger. For every event, the trigger reports the trigger decision as a bit mask (top half, bottom half or both) and the time the trigger fired. The turn-on from the trigger threshold was measured to be 1280 in units of ADC counts as expected. The threshold was not perfectly sharp because of uncertainties in the conversion from readout to trigger hits described above, but based on comparisons with simulation we found that the trigger worked exactly as specified.

7.4. Trigger Rate Comparisons

Trigger rates observed in the HPS Test Run are dominated by multiple Coulomb scattered e^+e^- pairs in the converter. In simulated events, the rate of triggers depend on the modeling of the pairs' angular distribution and the subsequent multiple Coulomb scattering in the converter. Rates from different converter thicknesses

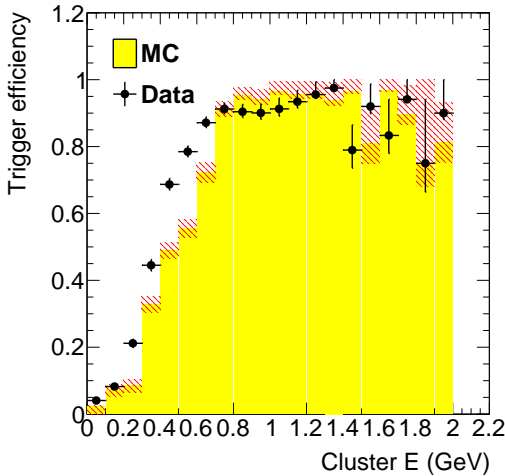


Figure 18: Trigger efficiency in both halves of the ECal for data and simulation as a function of cluster energy.

Converter (% X_0)	1.60	0.45	0.18
EGS5	1162 ± 112	255 ± 28	94 ± 17
Geant4	2633 ± 250	371 ± 38	114 ± 18
Observed	1064 ± 2	196 ± 1	92 ± 1

Table 4: Observed and predicted event rate (in Hz) normalized to 90 nA for three different converter thicknesses. The uncertainty on the prediction includes systematic uncertainties from ECal alignment, background normalization, beam current normalization and limited statistics in the simulation.

are used to study the varying multiple Coulomb scattering contribution (pair production angular distribution is constant), and are compared with Geant4 [24] standard multiple scattering model and EGS5 [25]. Restricting clusters to a well calibrated region of the ECal and subtracting the “no converter” background we see agreement with the rates predicted by the EGS5 simulation program, see Table 4. This gives further confidence that the dominant source of background occupancy for HPS, multiple Coulomb scattered beam electrons, is well described.

8. Summary and Outlook

The HPS Test Run experiment, using a simplified version of the apparatus planned for the full HPS experiment in a parasitic photon beam, demonstrated the feasibility of the detector technologies proposed for the silicon vertex tracker, electromagnetic calorimeter, and data acquisition systems. Performance from each of these subsystems has been shown to be adequate

to conduct the full experiment successfully with some identified improvements. Studies of multiple Coulomb scattering tails of electrons and positrons from photon conversions further backs expectations from simulation, giving credence to estimates of the detector backgrounds expected in electron beam running for HPS.

9. Acknowledgements

The authors are grateful for the support from Hall B at JLab and especially the Hall B engineering group for support during installation and decommissioning. They also would like to commend the CEBAF personnel for good beam performance, especially the last few hours of operating CEBAF6. The tremendous support from home institutions and supporting staff also needs praise from the authors.

This work has been supported by the US Department of Energy, the National Science Foundation, French Centre National de la Recherche Scientifique and Italian Istituto Nazionale di Fisica Nucleare. Rouven Essig is supported in part by the Department of Energy Early Career research program DESC0008061 and by a Sloan Foundation Research Fellowship. Authored by Jefferson Science Associates, LLC under U.S. DOE Contract No. DE-AC05-06OR23177.

9. References

- [1] B. Holdom, Two U(1)'s and Epsilon Charge Shifts, Phys.Lett. B166 (1986) 196.
- [2] P. Galison, A. Manohar, TWO Z's OR NOT TWO Z's?, Phys.Lett. B136 (1984) 279.
- [3] R. Essig, J. A. Jaros, W. Wester, P. H. Adrian, S. Andreas, et al. (Report of the Community Summer Study 2013 (Snowmass) Intensity Frontier New, Light, Weakly-Coupled Particles subgroup), Dark Sectors and New, Light, Weakly-Coupled Particles, 2013. URL: <http://arxiv.org/abs/arXiv:1311.0029>.
- [4] M. Pospelov, Secluded U(1) below the weak scale, Phys.Rev. D80 (2009) 095002.
- [5] O. Adriani, et al. (PAMELA Collaboration), An anomalous positron abundance in cosmic rays with energies 1.5-100 GeV, Nature 458 (2009) 607–609.
- [6] M. Ackermann, et al. (Fermi LAT Collaboration), Measurement of separate cosmic-ray electron and positron spectra with the Fermi Large Area Telescope, Phys.Rev.Lett. 108 (2012) 011103.
- [7] M. Aguilar, et al. (AMS Collaboration), First Result from the Alpha Magnetic Spectrometer on the International Space Station: Precision Measurement of the Positron Fraction in Primary Cosmic Rays of 0.5350 GeV, Phys.Rev.Lett. 110 (2013) 141102.
- [8] N. Arkani-Hamed, D. P. Finkbeiner, T. R. Slatyer, N. Weiner, A Theory of Dark Matter, Phys.Rev. D79 (2009) 015014.
- [9] M. Pospelov, A. Ritz, Astrophysical Signatures of Secluded Dark Matter, Phys.Lett. B671 (2009) 391–397.

- 947 [10] J. D. Bjorken, R. Essig, P. Schuster, N. Toro, New Fixed-Target
 948 Experiments to Search for Dark Gauge Forces, Phys.Rev. D80
 949 (2009) 075018.
- 950 [11] A. Grillo, et al. (HPS Collaboration), Heavy Photon Search
 951 Proposal, 2010. URL: https://confluence.slac.stanford.edu/download/attachments/86676777/HPSProposal-FINAL_Rev2.pdf.
- 952 [12] A. Sandorfi, et al., 2012. URL: http://www.jlab.org/exp_prog/proposals/06/PR06-101.pdf.
- 953 [13] F.-X. Girod, M. Garon (CLAS), Inner calorimeter in clas/dvcs
 954 experiment, CLAS-Note 2005-001 (2005).
- 955 [14] R. Niyazov, S. Stepanyan (CLAS), Clas/dvcs inner calorimeter
 956 calibration, CLAS-Note 2005-021 (2005).
- 957 [15] F.-X. Girod (Universite de Strasbourg), 2006. URL: <http://www.jlab.org/Hall-B/general/thesis/fxgirod.pdf>.
- 958 [16] I. Rashevskaya, S. Bettarini, G. Rizzo, L. Bosisio, S. Dittongo,
 959 et al., Radiation damage of silicon structures with electrons of
 960 900-MeV, Nucl. Instrum. Meth. A485 (2002) 126–132.
- 961 [17] D. S. Denisov, S. Soldner-Rembold, DO Run IIB Silicon Detec-
 962 tor Upgrade: Technical Design Report (2001).
- 963 [18] M. French, L. Jones, Q. Morrissey, A. Neviani, R. Turchetta,
 964 et al., Design and results from the APV25, a deep sub-micron
 965 CMOS front-end chip for the CMS tracker, Nucl.Instrum.Meth.
 966 A466 (2001) 359–365.
- 967 [19] M. Friedl, C. Irmler, M. Pernicka, Readout of silicon strip detec-
 968 tors with position and timing information, Nucl.Instrum.Meth.
 969 A598 (2009) 82–83.
- 970 [20] H. Dong, et al., Integrated tests of a high speed VXS switch
 971 card and 250 MSPS flash ADCs, 2007. doi:10.1109/NSSMIC.
 972 2007.4436457.
- 973 [21] R. Larsen, Emerging New Electronics Standards for Physics,
 974 Conf.Proc. C110904 (2011) 1981–1985.
- 975 [22] L. Jones, APV25-S1: User guide version 2.2, RAL Microelec-
 976 tronics Design Group, 2011.
- 977 [23] M. Friedl, C. Irmler, M. Pernicka, Obtaining exact time infor-
 978 mation of hits in silicon strip sensors read out by the APV25
 979 front-end chip, Nucl. Instrum. Meth. A572 (2007) 385 – 387.
- 980 [24] S. A. et al., GEANT4 - a simulation toolkit, Nucl.Instrum.Meth.
 981 A506 (2003) 250 – 303.
- 982 [25] H. Hirayama, Y. Namito, A. Bielajew, S. Wilderman, W. Nelson,
 983 The EGS5 Code System, 2005.